

# First results on characterization of Cerenkov images through combined use of Hillas, fractal and wavelet parameters

A. Haungs<sup>a</sup> A.K. Razdan<sup>b</sup> C.L. Bhat<sup>b</sup> R.C. Rannot<sup>b</sup>  
H. Rebel<sup>a</sup>

<sup>a</sup>*Forschungszentrum Karlsruhe, Institut für Kernphysik III, Postfach 3640,  
D-76021 Karlsruhe, Germany*

<sup>b</sup>*Bhabha Atomic Research Centre, Nuclear Research Laboratory,  
Mumbai - 400 085, India*

---

## Abstract

Based on Monte Carlo simulations using the CORSIKA code, it is shown that Cerenkov images produced by ultrahigh energy  $\gamma$ -rays and cosmic ray nuclei (proton, Neon and Iron) are fractal in nature. The resulting multifractal and wavelet moments when employed in association with the conventional Hillas parameters as inputs to a properly-trained artificial neural network are found to provide more efficient primary characterization scheme than the one based on the use of Hillas or fractal parameters alone.

*Key words:* Gamma rays; EAS; Composition; Cerenkov Technique  
*PACS:* 96.40.Pq, 98.70.Sa

---

## 1 Introduction

Recent developments on the simulation and experimental fronts in Cerenkov Imaging Technique (CIT) in the field of TeV  $\gamma$ -ray astronomy have made it possible to preferentially pick up atmospheric Cerenkov events from  $\gamma$ -ray progenitors and substantially reject cosmic-ray-generated background events ( $\gamma$ -ACE and C-ACE respectively, hereonwards) and thereby significantly augment the detection sensitivity of ground-based, very high energy (VHE)  $\gamma$ -ray telescopes [1]. For this purpose, a 2-dimensional Cerenkov image, as recorded by a fast photomultiplier tube (PMT)-based, multi-pixel camera, placed in

the focal-plane of a large light collector ( $\geq 10 \text{ m}^2$ ), is subjected to some pre-processing routines like 'flat-fielding' and 'cleaning' and is then parameterized as per the second- and higher-moments prescription proposed first by Hillas [2]. The resulting Hillas parameters, superceded by the supercuts image processing strategy, have helped to reject the C-ACE at  $\geq 99.7\%$  level, while permitting to retain the signal events ( $\gamma$ -ACE) at  $\sim 50\%$  level, leading, in turn, to a typical quality factor,  $Q$  of  $\sim 10$  for the prototype Whipple imaging Cerenkov telescope [3]. As this value appears to be close to the limiting  $Q$  that can be achieved through the use of moment-fitting procedures to the real or simulated Cerenkov images, the problem that warrants a serious attention now is whether a fundamentally different (and perhaps more primordial) image-processing approach can be found which will, on its own, or in conjunction with the presently-used image-analysis technique, help to classify the ACE progenitor more efficiently and thereby be able, not only to segregate  $\gamma$ - and C-ACE but also various primary cosmic-ray nuclear groups (different atomic number,  $Z$ , ranges), with respect to one another. While, on the one hand, this should enable the imaging Cerenkov telescopes to pick-up weaker  $\gamma$ -ray signals more quickly, on the other hand, it may also permit these instruments to function as a low-resolution cosmic-ray spectrometer, at least, to the extent of differentiating various cosmic-ray particles into low  $Z$  (Hydrogen or proton-like), medium  $Z$  (Neon-like) and high  $Z$  (Iron-like) nuclei. Thus, apart from performing  $\gamma$ -ray astronomy investigations, this may hopefully pave the way for deploying imaging Cerenkov telescopes eventually in a supplementary mode of operation for independent, cosmic-ray mass-composition studies in the ultra-high energy region – an important, outstanding problem in its own right, which is currently engaging lot of attention internationally. Motivated by this consideration, we investigate here the possibility of subjecting the Cerenkov image data to perhaps more general, albeit as-yet untried, multifractal and wavelet analyses in anticipation of deriving independent parameters which can supplement presently-in-use Hillas moments for event-characterization purposes. The paper discusses here first results from these exploratory studies, based on Cerenkov image data simulated for the Imaging Element of the 4-element TACTIC array, using the CORSIKA air-shower code.

## 2 TACTIC

The acronym TACTIC stands for a **T**eV **A**tmospheric **C**erenkov **T**elescope with an **I**maging **C**amera [4]. Keeping in mind the scientific merits of adopting the above-referred dual-purpose detection strategy, the TACTIC has been specifically designed, on one hand, to carry out high-sensitivity spectral and temporal investigations on VHE  $\gamma$ -ray sources on clear, dark nights and, on the other, to utilize it effectively during semi-lit portions of a night (nor-

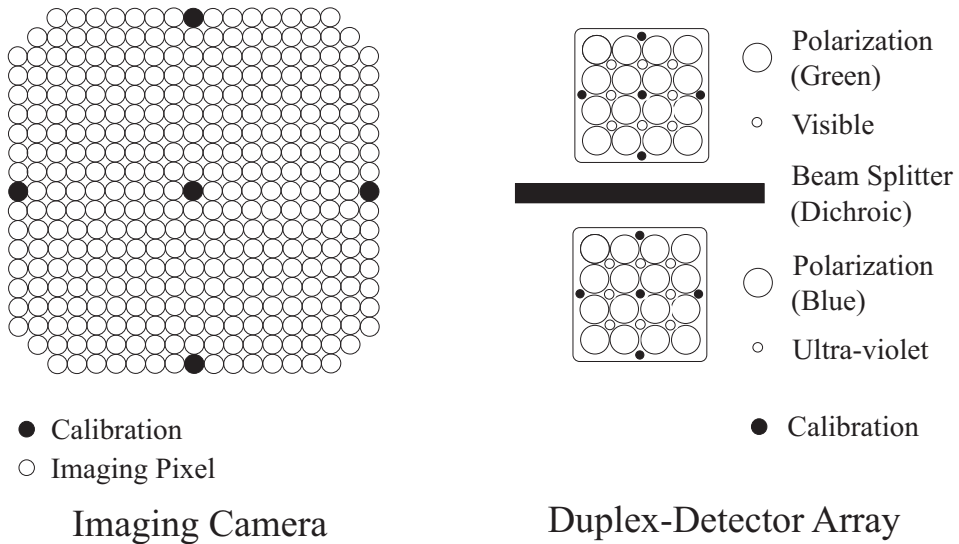
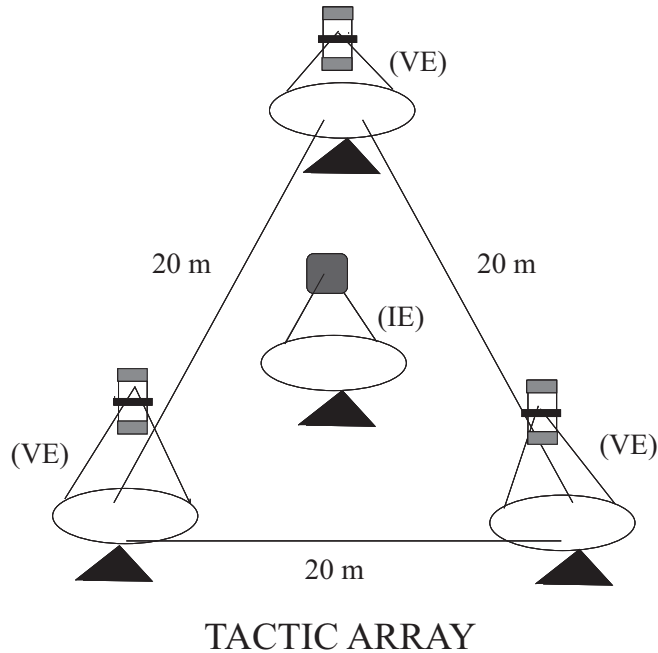


Fig. 1. Sketch of the TACTIC array and the cameras, presently under installation, for high-sensitivity spectral and temporal investigations on  $\gamma$ -ray sources in the photon energy range of  $\sim 0.5\text{--}10\text{ TeV}$  (details see text). The array would also investigate UHE cosmic-ray elemental composition (50-500 TeV per particle) in a supplementary mode of operations, going to be employed under partially moonlit conditions when normal  $\gamma$ -ray sources studied are not conventionally performed.

mally, shut-down period for atmospheric Cerenkov systems) for cosmic-ray mass-composition investigations in 10's-100's TeV particle energy region. This instrument consists of an array of 4 atmospheric Cerenkov elements each using a tessellated optical collector of  $9.5\text{ m}^2$  light collection area and a synchronized, computer-controlled alt-azimuth drive system. As is evident from

Fig.1, the Imaging Element (IE) of this compact telescope array is located at the centroid of an equilateral triangle of 20 m-side and the 3 Vertex Elements (VE) are placed at the vertices of this triangular configuration. The individual 60 cm-diameter mirror facets of the light collector are mounted so as to follow a quasi-Davis-Cotton surface profile, leading to an on-axis spot-size of  $\sim < 15$   $\mu$ m (FWHM). The IE has a fast photomultiplier tube (PMT)-based 349-pixel Imaging Camera in its focal-plane, covering a field-of-view (FoV) of  $\sim 6^\circ \times 6^\circ$  truncated square with a pixel resolution of  $\sim 0.31^\circ$  diameter. The 3 VE's, on the other hand, are provided with somewhat unconventional focal-plane instrumentation which consists of duplex PMT arrays of assorted sizes, placed across a beam-splitter/dichroic sheet assembly, as shown in Fig.1 . The resulting non-image parameters of the VE's are planned to be deployed in conjunction with the high-definition imaging data provided by the IE for a more efficient characterization of the recorded ACE in relation to the nature of the progenitor particles. The IE of the TACTIC is presently operational with a 81-pixel ( $9 \times 9$ ) camera and it is being regularly used since March 1997 for  $\gamma$ -ray source observations [5]. The 349-pixel IE of the TACTIC array is scheduled to become operational by December 1998. In anticipation of this commissioning schedule, comprehensive Monte Carlo simulation studies are presently underway to provide specific guidelines for optimizing event characterization strategies and thereby enable this instrument to carry out the above-outlined VHE  $\gamma$ -ray astronomy and UHE cosmic-ray mass-composition investigations through the atmospheric Cerenkov detection route. Here, in the first report on this work, we first establish that Cerenkov images recorded by an instrument like the TACTIC-IE for  $\gamma$ -ray, proton, Neon and Iron progenitors have a fractal structure, and then go on to demonstrate the feasibility of segregating these event families comparatively more efficiently by using Hillas parameters in association with a selection of multifractal dimensions and wavelet moments.

### 3 CORSIKA-based Cerenkov Image data-bases

The data-bases for carrying out the present feasibility-demonstration studies were generated using the CORSIKA (Version 4.5) air-shower code [6,7] with Cerenkov option, and the use of the high energy interaction model VENUS [8] and the model GHEISHA [9] for interactions at lower energies ( $E_{lab} < 80$  GeV). A rectangular matrix of  $60 \times 4$  detector elements, each  $5 \text{ m} \times 5 \text{ m}$  in dimensions, is folded into the CORSIKA simulation programme for this purpose, in conformity with the actual geometrical configuration of the TACTIC array and the size of its 4 light-collectors [10]. The Cerenkov data bases of 100 showers each for  $\gamma$ -rays, proton and Neon and Iron nuclei have been generated. These simulated data bases are valid for the altitude (1700 m) and magnetic

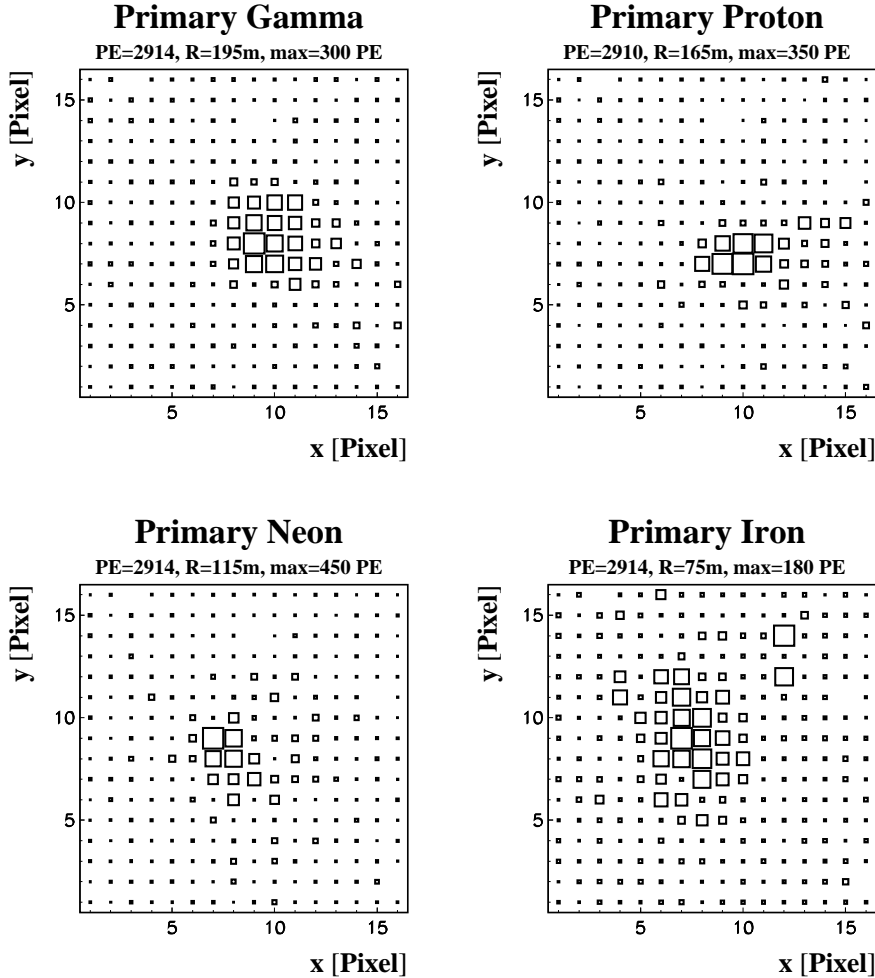


Fig. 2. *Examples of simulated Cerenkov images for a 16 x 16 pixel camera for different progenitors with approximately equal total number of photoelectrons (PE). The box size represents the number of PE per pixel, the number of PE for the largest pixel (max) is indicated as well as the distance R of the camera from the shower axis.*

field values of Gurushikhar, Mt. Abu, the permanent location of the TACTIC in the Western Indian state of Rajasthan. The zenith angle  $\Theta$  of the primary is fixed at  $40^\circ$  for gamma and  $40^\circ \pm 2^\circ$  for protons, Neon and Iron, larger  $\Theta$  being preferred to achieve twin benefits of a higher primary threshold energy and a larger effect collection area.  $\gamma$ -rays of energy 50 TeV and protons, Neon and Iron nuclei of 100 TeV energy (the factor of two higher energy for nuclear-progenitors being chosen to have roughly comparable average Cerenkov photon densities in all the 4 cases) have been considered. While  $\gamma$ -ray primaries are supposed to be incident along the principal axis of the TACTIC IE (as expected for  $\gamma$ -rays from a point-source) the 3 types of the cosmic-ray progenitors (protons, Neon and Iron) have their angles of incidence randomly oriented in a circular field of view of  $3^\circ$  radius around the IE axis

(in accord with the well-known isotropic angular distribution of cosmic rays). To keep computer time and the Cerenkov photon file size within manageable limits for a given event, the Cerenkov photons are generated in the restricted wavelength region,  $\lambda \sim (300 - 320)$  nm and simulation run bunch size has been fixed at 20 . Cerenkov photons likely to be received at a given element with  $\lambda$  outside the above-referred sample window are generated off-line, using the well-known Cerenkov radiation spectral law  $\sim \lambda^{-2}$ . Other exercises done subsequently in the off-line mode include (i) taking proper account of the  $\lambda$ -dependent atmospheric extinction suffered by the individual Cerenkov photons emitted in the overall wavelength interval  $\lambda \sim (300 - 600)$  nm, (ii) ray-tracing Cerenkov photons, incident on each 60 cm-diameter facet of the IE mirror into the focal-plane of the light receiver, and (iii) deriving the number of photo-electrons (PE) likely to be registered by each of the 349 photomultiplier (PMT) pixels of the IE camera after accounting for the reflection coefficient of the mirror and the quantum efficiency of the PMT pixels. Fig.2 gives representative examples of the images thus generated for the IE in response to 4 progenitor types ( $\gamma$ -particles, proton, Neon and Iron nuclei). In anticipation of the requirements of the associated analysis procedure, only the square-grid, comprising the innermost 16 x 16 pixels of the TACTIC imaging camera, has been considered. Each of these 256 pixels, (which also include the pixels with information on the simulated Cerenkov image) have been injected with a photomultiplier noise component  $\sim 4$  PE. The noise injected in the image follows Poissonian distribution. For each simulated event, there exist images corresponding to as many detector locations as folded to the CORSIKA output.

## 4 Classification Schemes

### 4.1 Hillas Image Parameters

The Cerenkov image recorded by a TACTIC-like imaging telescope represents the 2-dimensional distribution of the light pattern produced in the terrestrial atmosphere following the incidence therein of a VHE/UHE  $\gamma$ -ray or a cosmic-ray primary. This image has embedded in it signatures which relate to the details of interactions which the progenitor particle as well its secondary and higher-generation by-product particles undergo in the atmosphere. If properly interpreted, these signatures can be utilised to reveal the nature and the energy of the progenitor particle. Starting off with the pioneering work of Hillas, the effort so far has concentrated on approximating the image to a geometrical ellipse and parameterizing it in terms of some characteristic features like image 'shape' and 'orientation' with respect to a Cartesian frame of reference centred on the projection of the telescope axis on the image plane. Using the standard moments-fitting procedure [1], the typical parameters calculated for

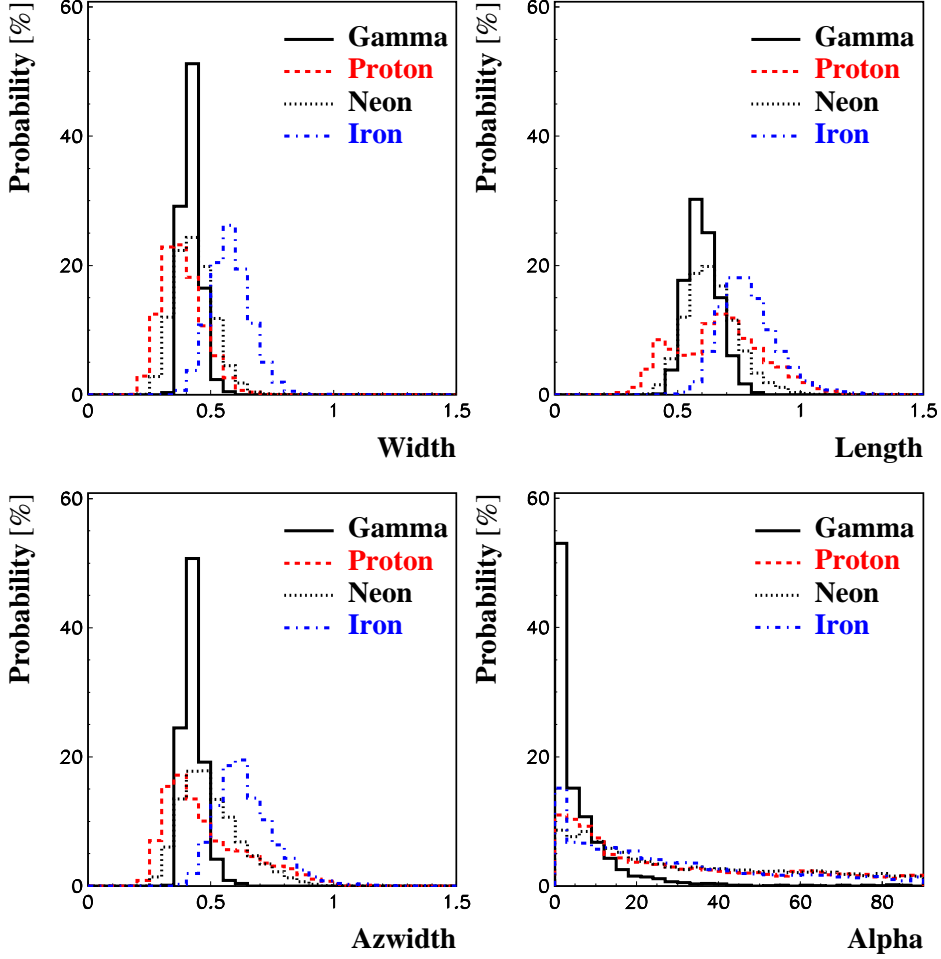


Fig. 3. Distributions of Hillas parameters for all simulated images in the range of PE from 1800 to 3000 for the different progenitor particles of the ACE.

each image ellipse are Length (L), Width (W), Azwidth (A), Miss (M), Alpha ( $\alpha$ ), Distance (D) as per the known formulae. Briefly stating here, the image Length and Width (shape parameter) refer to the dimensions of the major and minor axes of the projected ellipse and are related to the longitudinal and transverse developments of the associated Cerenkov radiation pulse. Similarly, the image 'orientation' parameter ( $\alpha$ ) gives a measure of the angular displacement of the major axis of the image from the line connecting the image centroid to the telescope axis. For a  $\gamma$ -ray event from an on-axis point source,  $\alpha$  is expected to be small, in practice generally  $\leq 10^\circ - 15^\circ$ , while for a cosmic-ray proton, all values of  $\alpha$  are equi-probable, in recognition of the isotropic angular distribution of cosmic-ray events. The results, obtained here for the IE of the TACTIC, using 4-component ( $\gamma$ , p, Ne and Fe) data-base, simulated as out-lined in section 3, are summarized in Fig.3 . As expected, all the plotted parameters are found to vary over a narrow range of values in the case of  $\gamma$ -rays as against the corresponding situation for the nuclear species because there exists a nuclear active channel where large transverse momenta may be

transferred to the pion secondaries, leading to a relatively broader Cerenkov image. Among the latter events, Fe images are found to have the narrowest distribution for most of the plotted parameters, which is a reflection of the fact that, for the same primary energy, an Fe shower reaches its peak growth at a higher altitude than a corresponding EAS induced by a lower Z primary, including a proton. However, it is evident from Fig.3 that there is a fairly high degree of overlap among the corresponding distribution profiles for an imaging parameter for these representative members of the cosmic-ray beam. Thus, speaking even qualitatively, it is apparent that, while Hillas image parameters can segregate  $\gamma$ -ACE from the C-ACE, they are not sufficiently sensitive to differences in Z and hence may not separate various nuclear progenitor types.

#### 4.2 *Multifractal and Wavelet Moments*

Pattern-analysis procedures, based on calculations of multifractal and wavelet moments of a structure, have started becoming popular now, for they are more holistic and permit a more detailed examination of the morphology of a structure on different length scales. These analysis techniques provide a set of robust classifiers which are more sensitive to the structure details and emphasize physical differences as against statistical fluctuations. Guided by these considerations, we show below that the present image data-base is amenable to the fractal and the wavelet treatments and, as an important consequence, it is possible to derive a set of independent parameters (multifractal and wavelet moments) with better potential for characterizing 4-component data-base used for illustration in the present work.

Fractals are structures which display a self similar behavior and fractal nature is quantitatively characterized by fractal dimension [11]. It is possible to calculate multifractal moments which quantify structures of multidimensional density distributions [12]. In anticipation of the requirements of the associated analysis procedure, only the square-grid, comprising the innermost 16 x 16 pixels of the TACTIC Imaging camera, has been considered. Noise has been added to check the robustness of these image processing techniques against deleterious effects by noise contamination. Only images with a total number of  $\geq 1800$  PE have been used. We have calculated multifractal moments of each simulated Cerenkov image by dividing the image into  $M = 4, 16, 64$  and 256 equally sized parts and by calculating the number of photoelectrons in each part.  $M$  is related to the fractal scale-length  $\nu$  by  $M = 2^\nu$ . The multifractal moments given by the following expression have been computed:

$$G_q(M) = \sum_{j=1}^M \left(\frac{k_j}{N}\right)^q, \quad N \neq 0, \quad (1)$$



where  $N$  is the total number of PE in the image,  $k_j$  is the number of PE in the  $j^{\text{th}}$  cell and  $q$  is the order of the fractal moment. If the Cerenkov image exhibits a self similar behavior the fractals moments  $G_q$  show a power law relation of the parameter of the length scale  $M$ :

$$G_q \propto M^{\tau_q} . \quad (2)$$

The exponent  $\tau_q$  is determined from  $G_q$  by using the formula given below

$$\tau_q = \frac{1}{\ln 2} \frac{d \ln G_q}{d \nu} . \quad (3)$$

The slope has been obtained from  $\nu = 1$  to  $\nu = 4$ . For a fractal structure, there exists a linear relationship between the natural logarithm of the multifractal moment ( $G_q$ ) and the fractal scale-length  $\nu$  and the slope of this line,  $\tau_q$  can be shown to be related to the generalized multifractal dimensions,  $D_q$  by

$$D_q = \frac{\tau_q}{q - 1} , \quad q \neq 1 , \quad (4)$$

where  $q$  is the order of the moment and varies over the range  $-6 \leq q \leq 6$ . For  $q = 1$ ,  $D_1$  is defined as equal to one. For purposes of illustration, the results of this analysis are shown in Figs.4-7 for one example each of  $\gamma$ -ray, proton, Neon and Iron events respectively, simulated as per the details given in section 3. The images of these 4 events, alongwith the injected noise, are shown in Fig.2, while the right and the left panels of Figs.4-7 respectively present plots of  $G_q$  vs.  $\nu$  and  $D_q$  vs.  $q$  for orders of the moments in the range

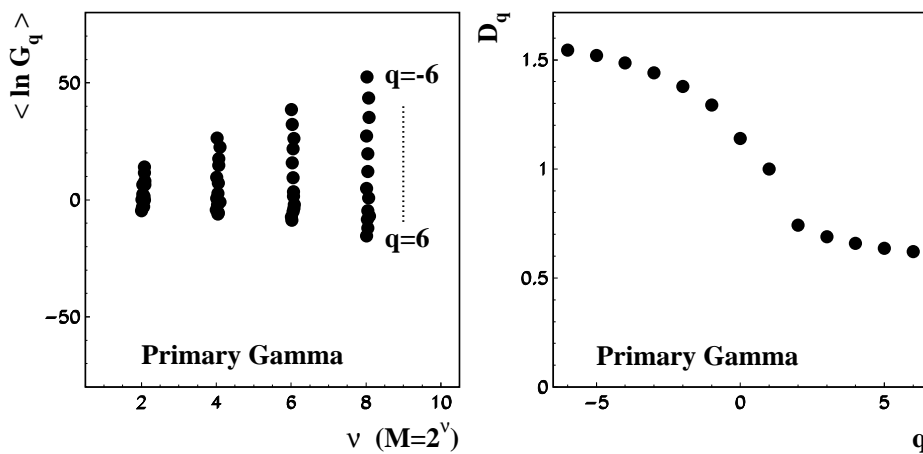


Fig. 4. Multifractal moments vs. length-scale  $\nu$  (left) and generalized multifractal dimensions vs.  $q$  (right) for one example of a  $\gamma$ -induced Cerenkov image displayed in Fig.2 .

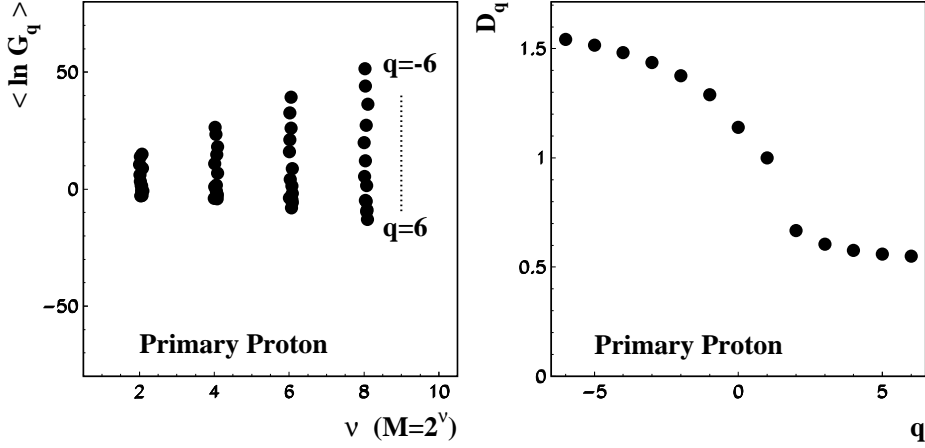


Fig. 5. Multifractal moments vs. length-scale  $\nu$  (left) and generalized multifractal dimensions vs.  $q$  (right) for one example of a proton-induced Cerenkov image displayed in Fig.2 .

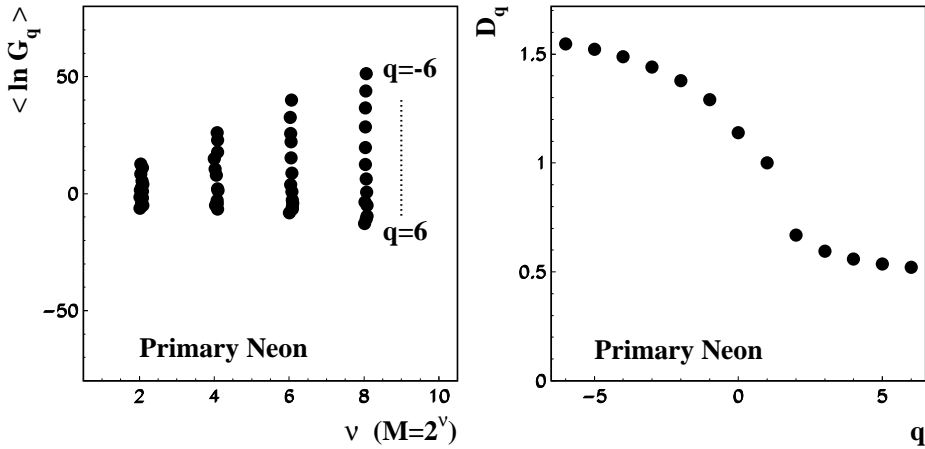


Fig. 6. Multifractal moments vs. length-scale  $\nu$  (left) and generalized multifractal dimensions vs.  $q$  (right) for one example of a Neon-induced Cerenkov image displayed in Fig.2 .

$-6 < q < 6$ . The power law relation of  $G_q$  vs.  $M$  is given in all images (i.e. the pattern has a self similar behavior) and therefore using the method of multifractal moments as parametrisation of the pattern is adaptable. This result is significant in that they establish that Cerenkov images produced by the 4 progenitor species, considered here, behave as fractals and as such their structures are amenable for analysis through use of multifractal dimensions  $D_q$ . A larger number of pixels at the camera would increase the usable length scale ( $\nu$ ) and therefore accuracy, but would not change the exponents  $\tau$  of the pattern. Another fractal feature is the saturation effected noted in the lower panels in the value of  $D_q$  with increasing  $q$ , thereby reassuring that the range  $-6 < q < 6$ , covered here is quite adequate. The value of  $D_{q_{max}}$  characterizes the location and the size of the largest irregularity in the image structure.

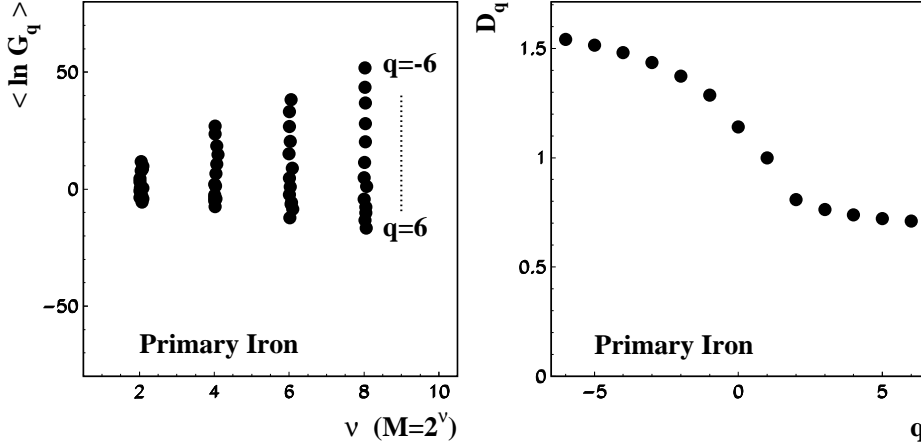


Fig. 7. Multifractal moments vs. length-scale  $\nu$  (left) and generalized multifractal dimensions vs.  $q$  (right) for one example of a Iron-induced Cerenkov image displayed in Fig.2 .

This means that, more regular the image, the closer is  $D_6$  to 1. On the other hand, the value of  $D_{q_{min}}$  refer to image zones with lower photoelectron density than the overall image size [13]. Due to the fact that, in the present case, the Cerenkov image generally does not fill the entire camera FoV of  $6^\circ \times 6^\circ$  and the sizes of the ellipses do not vary over a large range, values of  $D_q < 0$  are not useful in the present application.  $D_2$  is the so called correlation dimension [14], which is widely used in analysing experimental pattern distributions in terms of fractal dimensions. In Fig.8, we compare the distributions of the two

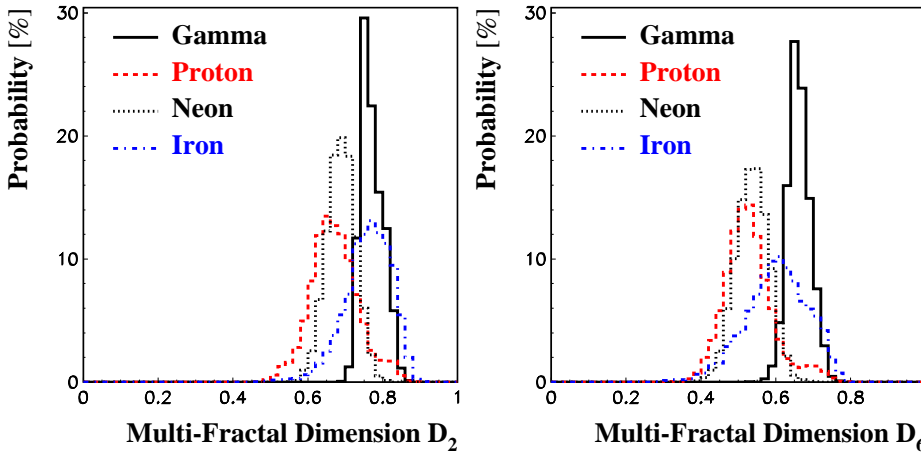


Fig. 8. Distributions of the multifractal dimensions  $D_2$  and  $D_6$  for all simulated images in the range of PE from 1800 to 3000 for the different progenitor particles of the ACE.

multifractal parameters  $D_2$  and  $D_6$  for the four progenitor species comprising the data-base used in the present work. Both families of the plotted curves indicate that the peak values of these two parameters are the smallest for protons and the largest values for  $\gamma$ -rays, with Neon followed by Iron images

having in-between values. This is essentially opposite to the behavior of the Length and Width Hillas parameters as is noted for these progenitor species in Fig.2. This is so because, while these two Hillas parameters are related to the image shape, the multifractal parameters  $D_2$  and  $D_6$  reflect the overall regularity of the image structure. As  $\gamma$ -ray images produce the most regular images amongst the four particle types considered here,  $D_2$  and  $D_6$  have the largest peak values for  $\gamma$ -ray progenitors. Iron images are more regular than proton images, since, for the same total energy per nucleus, iron events have lesser energy per nucleon. This results in a smaller interaction length for iron primaries (as in the case of  $\gamma$ -rays) and hence more secondaries with lesser energy for particle than what is expected in the case of proton events. This leads to destroy a visible hadronic core in the image of an Iron progenitor, while it survives in the case of a proton image. Using Hillas parameters  $\gamma$ -ray and proton images have a significant overlap in the corresponding distribution profiles, while Iron images are better segregated. Therefore, it follows that, by choosing a judicious combination of the Hillas and multifractal parameters, it should be possible to seek a better classification of these progenitor types.

By using wavelet analysis [15], which can be regarded as a sequence of versatile filtering processes which allows to examine an image for presence of local structures on different scale-lengths it has been possible to improve upon the results. Wavelet and wavelet transforms may be viewed as generalizations of the orthogonal Fourier transform. The wavelet analysis technique does not use a series of sine and cosine functions, as employed in the Fourier analysis, but a more localized functions, called wavelets, (e.g., Haar-wavelet). As such, the wavelets can detect both the location and the scale of a structure in an image. The wavelets are parameterized by a scale (dilation parameter)  $a > 0$  and a translation parameter)  $b$  ( $-\infty < b < +\infty$ ) such that

$$\phi(x) = \frac{\psi(x - b)}{a} . \quad (5)$$

The wavelet domain of one-dimensional function is rather two dimensional in nature; one dimension corresponding to the scale (a) and other corresponding to the space (translation b). Since we are analyzing a fractal; it is scaler rather than the translation that is of interest to us. When applied in the context of the TACTIC images, the wavelet moment [16]  $W_q$  is given by:

$$W_q(M) = \sum_{j=1}^M \left( \frac{|k_{j+1} - k_j|}{N} \right)^q \quad (6)$$

$k_j$  is the number of PE in the  $j^{th}$  cell in a particular scale, and  $k_{j+1}$  in the  $j^{th}$  cell in the consecutive scale. The wavelet moments have been obtained by

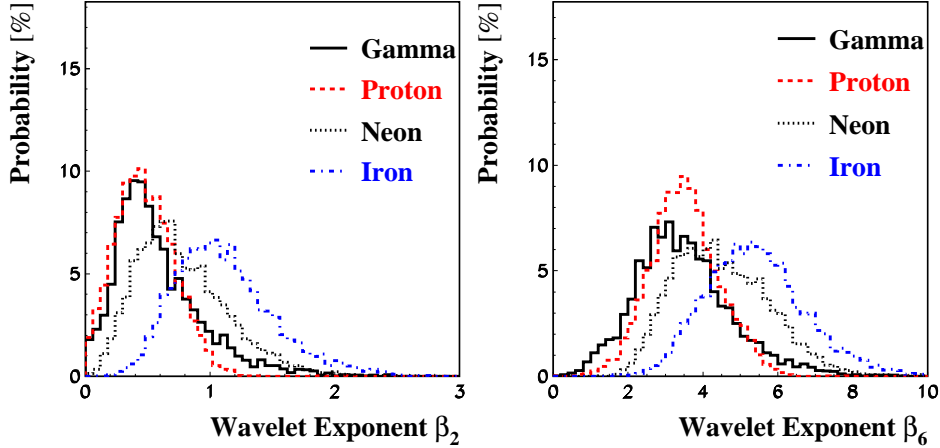


Fig. 9. Distributions of the wavelet parameters  $\beta_2$  and  $\beta_6$  for all simulated images in the range of PE from 1800 to 3000 for the different progenitor particles of the ACE.

dividing the Cerenkov image into  $M = 4, 16, 64, 256$  equally sized parts (with 64, 16, 4, 1 PMT, respectively) and counting the number of photoelectrons in each part. The difference of probability in each scale gives the wavelet moment. Again a proportionality

$$W_q \propto M^{\beta_q} \quad (7)$$

is given for the electron distribution in the Cerenkov images. The two wavelet dimensions which we have used for examining the structures of the Cerenkov images are the slopes  $\beta$  of the best-fit regression line for the double logarithmic distribution  $W_q$  vs.  $M$  for  $q = 2$  and  $q = 6$  obtained for each image. Fig.9, gives the distribution of these two wavelet parameters  $\beta_2, \beta_6$  for the simulated data-bases and belonging to the 4 progenitor species used in this work:  $\gamma$ -rays, protons and Neon and Iron nuclei. The steepness of the slope is found to gradually increase from gamma-rays to protons, followed by Neon and Iron nuclei. It is well known that wavelet moments are sensitive to differences in the average numbers of photoelectrons in neighboring pixels on different length scales. Lesser this difference, i.e., more regular the image, the flatter is the slope of the best-fit ( $\ln W_q$  vs.  $\ln M$ ) regression line. As Fe and Ne events are associated with a relatively larger number of muons compared with proton (and  $\gamma$ -ray) events, the Cerenkov images produced by these high  $Z$  nuclei are characterized by local intensity peaks, resulting in higher values for the slope parameter in case of high  $Z$  nuclei compared with protons (and  $\gamma$ -rays). This feature, which may be present in the structure of a Cerenkov image, is not readily exploitable through the conventional route, i.e., the use of Hillas parameters. This underlines the possible role of the wavelet parameters is being used as a supplementary set of parameters for better event-characterization purposes.

### 4.3 Artificial Neural Network-based Classification

We use the well known pattern recognition capabilities of an artificial neural network (ANN), in order to display the degree by which the event-classification potential of the Hillas parameters can be increased through the supplementary use of the fractal and wavelet parameters. From a statistical modeling point of view, the ANN technique represents a non-parametric event classification scheme. As it contains more free parameters, it requires relatively more training data. On the other hand, it is faster and more fault-tolerant and in

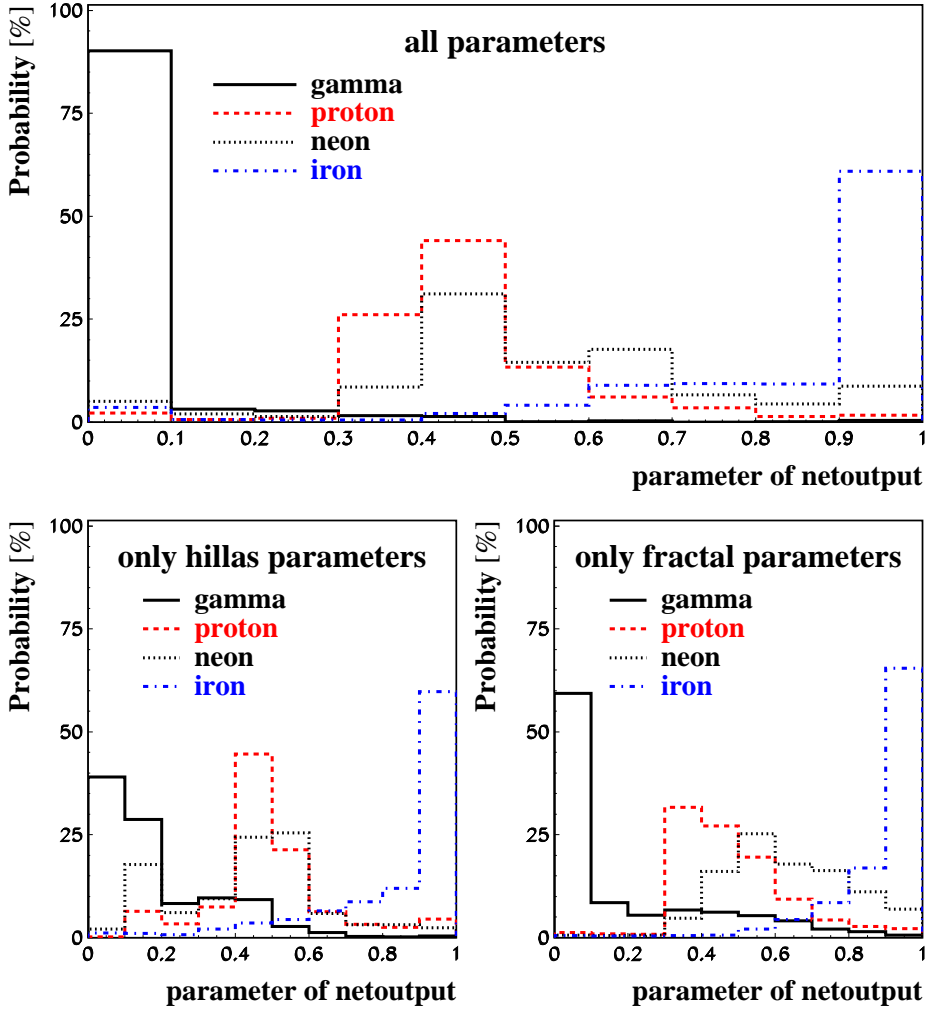


Fig. 10. Distributions of the different primaries in the output parameter of neural nets with different sets of parameters. The nets are trained with an independent event sample. Demanded output values are 0., 0.33, 0.67, 1. for primary  $\gamma$ ,  $p$ , Ne, Fe respectively.

that sense is expected to yield better results than other multivariate analysis techniques presently in use for present exploratory exercise. We have used the jetnet 3.0 ANN package developed by Lönnblad et al. [17]. The transfer

function used is of the sigmoid type  $\sim (1 + \exp(-2n))^{-1}$ . Two hidden layers were used with backpropagation mode in this exercise alongwith optimized learning parameters. A sample of 12000 events was used during the training session of the network and the output values demanded are 0.0 for  $\gamma$ -rays, 0.33 for protons, 0.67 for Neon nuclei and 1.0 for Iron nuclei. The test data set comprises a total of 24000 events, belonging to  $\gamma$ -ray, proton, Neon and Iron species, all 4 in an equal proportion. First, the network was trained with only Hillas parameters, viz., L, W, A, and  $\alpha$ . There is a clear distinction between  $\gamma$  and hadron induced showers. However, among hadrons, proton and the Neon distributions significantly overlap and the Iron component is relatively better separated as shown in Fig.10 .

In the second exercise, two fractal ( $D_2$  and  $D_6$ ) and two wavelet ( $\beta_2$  and  $\beta_6$ ) parameter values have been used as inputs to the net and it is clear from Fig.10 that  $\gamma$ -rays and hadrons are again well separated, but among hadrons, Neon and proton distributions are less overlapped while Iron is very well separated. In the final ANN approach, Hillas parameters, fractal parameters (two) and wavelet parameters (two) are used in tandem in the input, again each with 12000 events of training and 24000 events of testing. The results are illustrated in Fig.10 where progenitor species, particularly  $\gamma$ -rays and Fe nuclei prove to be better separated from each other and also from proton and neon events compared with the procedures based on Hillas or fractal/wavelet parameters alone. Similar results are obtained by using different harder and softer cuts on the number of PE for the training and generation samples. This largely precludes systematic effects which could be due to the small size of the shower sample simulated by CORSIKA. With increasing number of parameters an increasing number (squared) of simulated events for the training is required, thus for the combined training (Fig.10 upper panel) the present number of simulated events seem to be small. An iterative way of using neural nets is therefore promising, i.e. in a first step a separation of  $\gamma$  to all hadrons and, afterwards, a neural net analysis for the separation of different charges of the hadronic cosmic rays.

Addressing finally the question what are the merits of the fractal approach in analysing the images, as compared to the standard procedures, one has to specify the detailed case and the aim of the analysis. For example, if the analysis intends to prepare high purity samples of  $\gamma$ -events at the expense of efficiency or a classification of all registered events in different primary mass groups with a reliable mapping of the mass composition, varying strategies have to be employed and the optimum method has to be dedicatedly explored.

## 5 Discussion

The possibility of using the TACTIC telescope to study the mass composition of cosmic rays in UHE region has motivated us to look for non-traditional approaches for parameterization of the Cerenkov image. Proton is the main cosmic ray component which bombards the upper layer of the atmosphere.  $\gamma$ -ACE have comparatively lesser transverse development all through their passage in the longitudinal direction as compared with the corresponding situation in hadronic showers. The result is that Cerenkov light-producing charged components ( $e/\mu$ ) are carried more closer to the ground level for hadronic showers and there is intense pool of Cerenkov light close to the shower axis. The electromagnetic processes in the hadronic showers are sustained by neutral-pion decay through  $\pi^0 \rightarrow \gamma + \gamma$ . On the other hand, muons resulting from decay of  $\pi^\pm$  may have large transverse momenta imparted to them. These muons, on reaching the ground level, produce local peaks in the overall Cerenkov lateral distribution profile. For ACE due to Neon and Iron nuclei, there is a large content of these muons and consequently Cerenkov image structure may be more diffuse than that in the case of protons. Hillas parameters are significantly sensitive to distinguish  $\gamma$ -rays from the overall family of hadrons, but, as shown here, not good enough for efficient segregation of various Z groups in the cosmic-ray beam. One reason for multifractal moments to be effective as classifiers is because, as shown here, Cerenkov images are multidimensional patterns and therefore they can be analyzed and parametrized by common pattern recognition methods like fractals or wavelets. The resulting parameters are sensitive to different physical features of the images, i.e. the shower development in the atmosphere. On the other hand, the reason why wavelet moments also seem to have an excellent potential as additional research tool is that they search for differences in photon density gradients of the Cerenkov image. The image profile gets more diffuse when we go from proton onwards to the iron component as the muon content also increases accordingly. The effect of the muon content on the Cerenkov image is to diffuse the structure. It seems to be properly taken into account by fractal and wavelet moments.

## 6 Conclusions

It has been shown here that Cerenkov images have a fractal structure. As a first follow-up of this important realization, it is also indicated that multifractal dimensions and wavelet moments can be used alongwith Hillas parameters to discriminate more efficiently amongst gamma-rays, protons, Neon and Iron progenitor species through the use of a properly-trained artificial neural net. Multifractal and wavelet approach for analyzing Cerenkov images has been discussed for the first time in gamma-ray astronomy and this (preliminary) work



suggests that the outlook for using the resulting parameters as supplementary classifiers for cosmic-ray mass-composition studies in the UHE bracket is quite encouraging.

## Acknowledgements

The work is embedded in the Indian-German bilateral agreement of scientific-technical cooperation (WTZ INI-205).

## References

- [1] D.J. Fegan, J. Phys. G: Nucl. Part. Phys. **23** (1997) 1013
- [2] A.M. Hillas, Proc. 19<sup>th</sup> ICRC (La Jolla) **3** (1985) 445
- [3] T.C. Weekes et al., Astrophys. J. **342** (1989) 379
- [4] C.L. Bhat et al., "Towards a Major Atmospheric Cerenkov Detector-III", Universal Academic Press 1994, ed. T. Kifune, p. 207
- [5] C.L. Bhat, Rapporteur Talk at the 25<sup>th</sup> ICRC (Durban), World Scientific 1997, eds. M.S. Potgieter, B.C. Raubenheimer, D.J. van der Walt, p. 211
- [6] J.N. Capdevielle et al., KfK-Report 4998, Kernforschungszentrum Karlsruhe (1990)
- [7] D. Heck, J. Knapp, J.N. Capdevielle, G. Schatz, T. Thouw, FZKA-Report 6019, Forschungszentrum Karlsruhe (1998)
- [8] K. Werner, Phys. Rep. **232** (1993) 87
- [9] H. Fesefeldt, Report PITHA 85/02, RWTH Aachen, Germany (1985)
- [10] R.C. Rannot et al., Nucl. Phys. B (Proc. Suppl.) **52B** (1997) 269
- [11] B.B. Mandelbrot, Journ. Fluid Mech. **62** (1974) 331
- [12] A. Aharony, Physica **A 168** (1990) 479
- [13] A. Haungs, J. Kempa, H.J. Mathes, H. Rebel, J. Wentz, Nucl. Instr. Meth. A **372** (1996) 515
- [14] H.G.E. Hentschel, I. Procaccia, Physica **D 8** (1983) 435
- [15] I. Daubechies, Commun. Pure Appl. Math. **41** (1988) 909
- [16] J.W. Kantelhardt, H.E. Roman, M. Greiner, Physica **A 220** (1995) 219
- [17] L. Lönnblad, C. Peterson, T. Rönigvaldsson, CERN Preprint, CERN-TH. 7135/94 (1994)